Accurate Prediction of the Wall Shear Stress in Rod Bundles with the Spectral Element Method at High Reynolds Numbers

Justin Walker, Elia Merzari, Aleks Obabko, Paul Fischer, and Andrew Siegel

E-mail: emerzari@anl.gov

Mathematics and Computer Science Division, Argonne National Laboratory

June 25, 2013

Abstract

Wall-bounded flows at high Reynolds number are characterized by high rates of shear at the walls. Resolving the flow near the wall, is critical to correctly reproducing the turbulence. In the present paper, we show that the accurate prediction of spatially varying wall shear stress requires additional near-wall resolution for large eddy simulation. We also demonstrate the advantage of the use of higher order polynomials for such calculations. The difficulties of resolving derivatives in a weak formulation are considered. A large eddy simulation of a channel flow is performed in order to examine these difficulties in a canonical flow. The dependence on resolution and subgrid-scale models is investigated. Results are compared with direct numerical simulation. A large eddy simulation of a single rod in a periodic array at Re = 64590 is performed. The results of h-refinement and p-refinement are compared. Wall shear stress and additional results are compared with experimental data. Implications for rod bundle calculations are discussed.

1 Introduction

Accurate prediction of wall shear stress is critical in the analysis of turbulent wall-bounded flows [24]. It is important for the production of correct friction factors, turbulent kinetic energy production, the analysis of heat transfer, and study of fluid-structure interaction. In most flows of engineering interest, the wall shear stress and viscous stresses are nonuniform since they are functions of the velocity derivatives. In order to predict the wall shear stress correctly, the regularity and smoothness of the velocity solution need to

be guaranteed. However, in methods that solve the weak form of the Navier-Stokes equation such as the spectral element method (SEM), the space of solutions is usually chosen to be less regular than C^1 so that only weak derivatives are guaranteed to exist, and the derivatives do not have the same strict requirement to converge that the solution does [5]. While approximations of the convergence of derivatives exist, we are interested in what is seen in practice, especially in the case of underresolved, non-DNS (direct numerical simulation) flows. We aim to provide guidelines to predict wall shear stress in complex engineering flows at realistic Reynolds numbers while maintaining the mesh resolution as coarse as possible. The target problem chosen is the parallel flow in rod bundles.

The prediction of the flow in rod bundles is of fundamental importance in a variety of engineering fields. It is, for instance, relevant for heat transfer applications such as the design of tube and shell heat exchangers as well as nuclear reactor core analysis. In nuclear reactor cores, the heat produced by the nuclear fuel contained within the rods is removed by the coolant flowing through the bundle. To predict with greater accuracy the behavior and the thermal performance of nuclear reactors, one must to better understand the underlying hydrodynamics.

Rod bundle flows differ significantly from pipe flow and parallel channel flow [13, 25, 31]. Rod bundles present flow characteristics that are reminiscent of external flows. Viscous dissipation and wall shear stress change azimuthally. Coherent structures might develop in the streamwise direction for particularly tight bundles. Moreover, the flow anisotropy induces secondary flows.

Especially important for nuclear engineering applications is the prediction of the peak fuel temperature and peak fluid temperature. Ideally, one would compute a temperature solution by prescribing a heat flux at the boundary or, even better, by performing a conjugate heat transfer calculation. In cases where that is not possible, the Reynolds analogy can be used to obtain an approximation to the heat transfer from known values of the wall shear stress.

RANS models developed for internal flows do not usually fare well for rod bundles because of a combination of the previous points [1, 19]. Accounting for more physics and reasonable tuning leads to better results. However, a more general approach such as large eddy simulation (LES) is desirable to lead to better predictability and freedom in exploring the design space [18]. In LES the large scales of turbulence are resolved while the small scale contribution to dissipation is modeled. Wall-resolved LES presents significant advantages when considering conjugate heat transfer calculations. Moreover, it permits exploring the physics of near-wall turbulence, which dramatically influences heat transfer. Traditionally, wall-resolved LES has been limited to relatively low Reynolds numbers since the computational cost scales with the Reynolds number.

One of the purposes of the present work is to test such methodology at Reynolds numbers of engineering interest and to verify how coarse the grid can be. As part of the Center for the Exascale Simulation of Advanced Reactors (CESAR) [30] effort, increasingly large simulations are planned comprising full reactor cores, and accessing the minimal computational requirements is fundamental importance.

The code used for all the calculations performed for the present work is Nek5000 [7, 9], a developed at Argonne National Laboratory and the target CFD code of CESAR. Nek5000 has demonstrated excellent parallel performance on petascale level machines when at least 20,000 collocation points are allocated per MPI process. Nek5000 solves the incompressible Navier-Stokes equations in the weak form using the spectral element method, a higher-order method in space.

In the present paper we explore the computational requirements to perform LES simulations at high Reynolds numbers in rod bundles using Nek5000. The objective is to be able to perform full bundle simulations at the Reynolds numbers encountered in prototype reactors ($\sim$70,000) with the least amount of computational effort possible while maintaining excellent accuracy for both velocity distribution and wall shear stress. This implies operating LES at the limit of underresolution, where the method does not guarantee a smooth solution of the derivatives. An approach to locally increase the resolution was found to be required in order to correctly resolve the wall shear stress. In fact, in order to achieve accurate prediction of wall shear stress in an LES, resolution requirements are greater than what is needed for other measures of accuracy such as the law of the wall.

Preliminary results for a 37-rod bundle simulation, performed by using the resolution guidelines described in the present work, are shown in Figure 1. The grid resolution studies presented in this work have been performed on an infinite array (Figure 1d) for simplicity and reduced computational cost.

In Section 2, the computational methodology is summerized. In Section 3 the issues concerning wall shear stress are described in more detail. Section 4 contains a systematic study of the effects of underresolution on the mean flow quantities in the case of channel flow. Section 5 focuses on the target case, the parallel flow in rod bundles. The results of several calculations are compared and conclusions drawn about best practices.

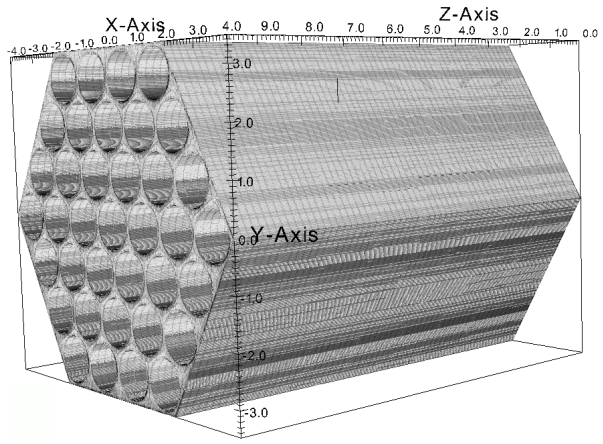

(a) Mesh for the 37-rod bundle case

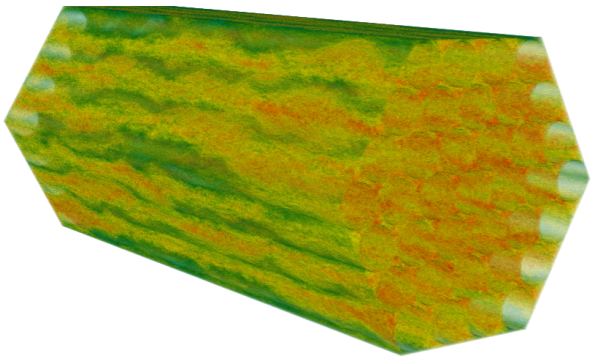

(b) Volume rendering of the streamwise velocity

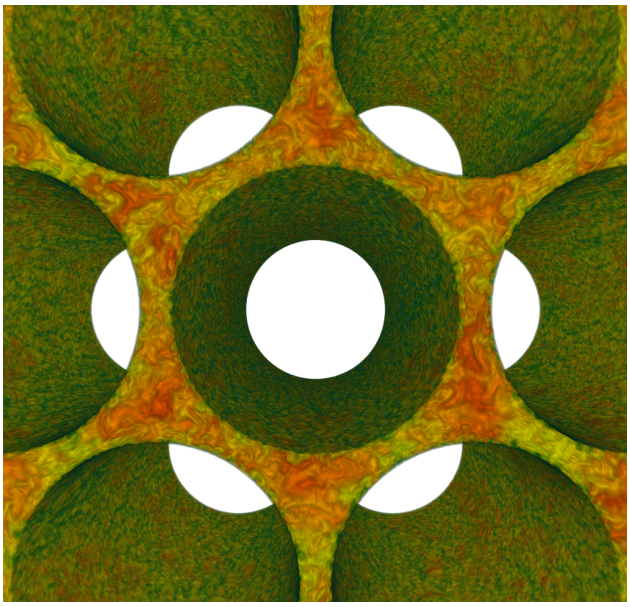

(c) Volume rendering of the streamwise velocity, detail

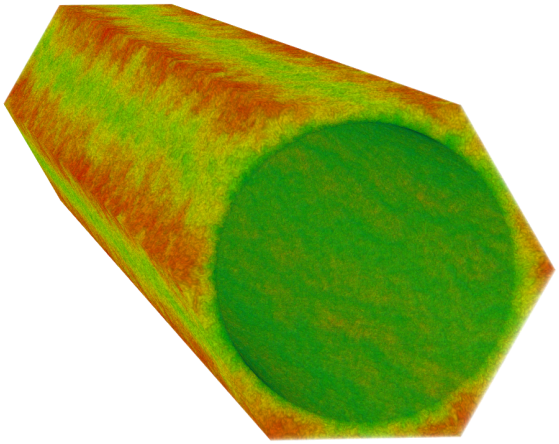

(d) Volume rendering of the single rod arrangement

Figure 1: Results of a 37-rod bundle case.

2 Methodology

Calculations were performed by using the spectral element code Nek5000 [9]. Nek5000 solves the incompressible Navier-Stokes equations.

In this study the incompressible Navier-Stokes equations are solved in their standard Cartesian form:

$$\frac{\partial u_i}{\partial t} + u_j \frac{\partial u_i}{\partial x_j} = -\frac{\partial p}{\partial x_i} + \frac{1}{\mathrm{Re}} \frac{\partial^2 u_i}{\partial x_j \partial x_j} \tag{1a}$$

$$\frac{\partial u_i}{\partial x_i} = 0 \tag{1b}$$

along with appropriate boundary conditions. All variables have been nondimensionalized by a characteristic length δ and velocity scale U; Re is the Reynolds number.

The domain and equations are discretized following the form of the spectral element method. The spectral element method solves the Navier-Stokes equations on a given domain by discretizing the solution space into elements such that the global solution is composed of piecewise polynomial functions with compact support. The problem is solved as a variational problem in what is known as weak form [5]. (More details are given in Section 3.) Lagrangian polynomial functions of up to the 23rd degree have been used to discretize the velocity field in each element in the present work. In the generalized, weighted residual framework, the present spectral-element method can be classified as a Galerkin method where the test functions and the basis functions for each element are Lagrange polynomials evaluated on Gauss-Lobatto-Legendre collocations points for the velocity. The pressure is solved with the same order polynomials as the velocity (P_N-P_N formulation).

Equations (1a) and (1b) are integrated in time by using a characteristic scheme as described by Maday et al. [17]. This method avoids the Courant-Friedrichs-Lewy (CFL) stability constraint in typical semi-implicit timestepping implementations, allowing greater time steps with CFL values in the range of 3-4.

In all problems considered here, periodic boundary conditions are applied in the streamwise direction. A dynamic forcing term is calculated at each time step to ensure a fixed flow rate.

The LES calculations carried out in this study use the stabilizing filter of Fischer and Mullen [8]. In this method, the solution at each time step is explicitly filtered. The filter operator F_α is defined as

$$F_\alpha := \alpha I_{N-1} + (1-\alpha)\mathbf{I}, \tag{2}$$

where $\mathbf{I}$ is the identity operator and I_N is the interpolation operator at the $N+1$ GLL nodes. This filter has the desirable property that it preserves the spectral convergence of SEM. As $N \to \infty$, the interpolation error goes to zero exponentially.

3 Wall Shear Stress

Nek5000 solves the Navier-Stokes equations using the weak formulation. Given a boundary value problem on a domain Ω with a solution $u \in V$,

$$D[u(x)] = f, \qquad x \in \Omega, \tag{3}$$

where D is a differential operator, one can recast the equation the problem in a variational form [5], also know as the weak formulation. In this form, one wants to find $u \in V$ such that

$$(Du, v) = (f, v), \qquad \forall v \in V, \tag{4}$$

where $(\cdot, \cdot)$ is a suitable inner product and v is a test function. One generally chooses the solution space $V \subset H_0^1(\Omega)^d$, which is the Sobolev space of functions in L^2 that vanish on the boundary and whose first derivatives are in L^2, where d is the dimension.

In applications, one generally uses analytic functions of either polynomials or trignometric functions to approximate the unique solution $\hat{u}$. Let $\{V_N\}_{N=0}^{\infty}$ represent a family of finite-dimensional subspaces that cover V. We then look for approximate solutions $u_N \in V_N$. With Galerkin methods, such as SEM, the solution space is $V_N := \mathbb{P}_N(\Omega)$, the space of polynomials of order N.

The choice of V has implications for the error of the approximate solution and, more important, its derivative, as found by the weak form of the problem. Sobolev embedding theorems [**?**] tell us that the Sobolev space given by

$$W^{1,p}(\Omega) := \left\{ v \in L^p(\Omega) : \frac{\partial v}{\partial x_i} \in L^p(\Omega), i = 1, \ldots, d \right\} \tag{5}$$

is embedded $W^{1,p}(\Omega) \subset C(\Omega)$ as long as $p > d$. This case obviously holds for $d = 1$, implying that all solutions are continuous. Less regularity holds for $d \geq 2$, since the existence of finite L^p norms for $p > 2$ cannot be guaranteed.

The approximation error from using a truncated polynomial expansion for $d = 1$, as in SEM, is given as follows. For any element $u \in H_w^1(\Omega)$, the truncated Legendre polynomial expansion $P_N u := \sum_{k=0}^{N} \hat{u}_k p_k$ converges [5] as

$$\|u - P_N u\|_{L_w^2(\Omega)} \leq C N^{-m} \|u\|_{H_w^m \Omega}. \tag{6}$$

More important for the current discussion is the approximation error for the derivatives $(\cdot)_x := \partial(\cdot)/\partial x$ given by

$$\|u_x - (P_N u)_x\|_{L^2_w(\Omega)} \approx C N^{3/2-m}, \tag{7}$$

which means that if $u \in H^1_w(\Omega)$, but $u \notin H^2_w(\Omega)$ then $(P_N u)_x$ does not necessarily converge to u_x. The scenario is even worse for $d \geq 2$.

The wall shear stress is defined by

$$\tau_w := [(\tau_{ij} n_j)^2 - (\tau_{ij} n_i n_j)^2]^{\frac{1}{2}}, \tag{8}$$

where n is the unit normal of a boundary surface and τ_{ij} is the stress tensor, defined as

$$\tau_{ij} = \mu \left(\frac{\partial u_i}{\partial x_j} + \frac{\partial u_j}{\partial x_i} \right), \tag{9}$$

where μ is the dynamic viscosity. When there is spanwise homogeneity, such as in the case of turbulent channel flow, the definition of the wall shear stress simplifies to another standard form,

$$\tau_w = \mu \frac{\partial u}{\partial n}, \tag{10}$$

where n is the normal direction to a boundary.

The results from this section highlight the difficulty of correctly reproducing the wall shear stress. Since the wall shear stress is derived from derivatives of the solution, it is important that these be correct. In particular, in a weak formulation, where regularity of the derivatives is not guaranteed, the resolution requirements to resolve the derivatives of the solution may be more stringent than those to resolve the solution to a given level of accuracy.

4 Channel flow

The effects of underresolution on the wall shear stress were investigated in the canonical case of turbulent channel flow. We compare the results of high and low amounts of filtering and of higher-order and lower-order spectral elements. Channel flow has been studied extensively at low Reynolds numbers. For example, two calculations are the DNS by Kim, Moin, and Moser [15] with Re = 3300 and the DNS of Moser, Kim,

and Mansour [22] with Re = 10935, hereafter KMM and MKM, respectively. We will compare our results with the higher Reynolds number study of MKM.

The focus section of these comparisons in this is the local wall shear stress as a function of the spanwise position, which is the relevant quantity of interest for rod bundle flows.

4.1 Numerical Model

The domain of the problem is a rectangular channel periodic in the streamwise and spanwise directions, x and z, respectively. The last two boundaries, normal to the y axis at $y = \pm\delta$, have the no-slip boundary condition applied. All quantities have been nondimensionalized by the channel half-width δ and mean streamwise velocity U. The streamwise and spanwise dimensions of the domain are chosen to be $2\pi\delta$ and $\pi\delta$, respectively. The bulk Reynolds number is $\mathrm{Re} = \delta U/\nu$, where ν is the kinematic viscosity. The boundary layer Reynolds number is defined as $\mathrm{Re}_\tau = u_\tau\delta/\nu$, where u_τ is the shear velocity.

The bulk Reynolds number was chosen to be Re = 10935, which corresponds to $\mathrm{Re}_\tau = 590$ as in MKM. Although the domain streamwise and spanwise dimensions were half those in MKM, the effects of underresolution under investigation are unrelated to the domain reduction. In the most resolved case, the results for the mean flow are close to those of MKM.

All cases have been averaged over an advective time of at least $500\,\delta/U$ at a time step of $\Delta t = 0.02\,\delta/U$. In addition, quantities were averaged over statistically homogeneous directions, x and z, and about the plane of symmetry $y = 0$.

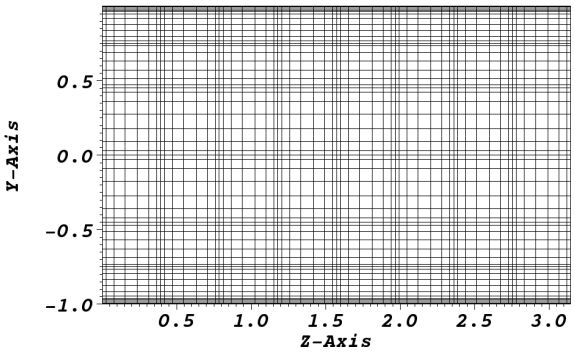

(a) M1: Cases A, B, H, I, J. $(8, 8, 8; 7)$

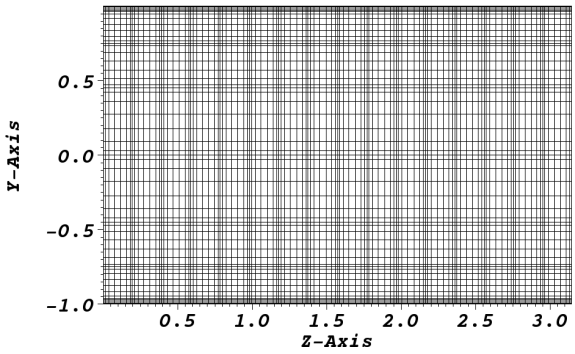

(b) M2: Case C. $(8, 8, 16; 7)$

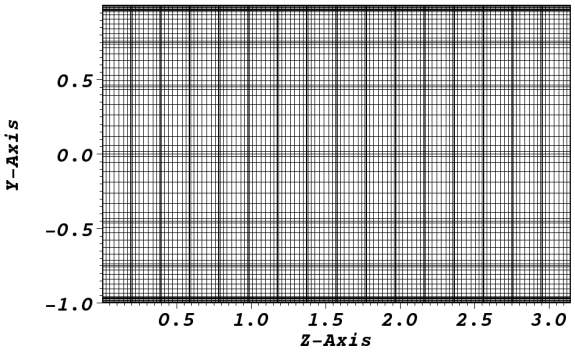

(c) M3: Cases D, E, F, G. $(8, 8, 16; 9)$

Figure 2: Meshes for channel flow with $(E_x, E_y, E_z; N)$.

4.2 Results

In this section we consider how varying parameters of the computational method affect the solution: first, the Nek5000 filter parameters; second, spanwise resolution; third, streamwise resolution; and fourth, explicit SGS models.

Table 1: Channel flow parameters for setups studied.

$\mathrm{Re} = 10935,\ \mathrm{Re}_\tau = 590$										
E_x	E_y	E_z	N	$\Delta x^+_{\max}$	y_1^+	$\Delta z^+_{\max}$	$\tau_{w,m}(\times 10^{-3})$	$\Delta\tau_{\max}$	$\alpha,\ M$	Case
8	8	8	7	96.5	1.5	48.2	2.46	0.28	0.05, 2	A
8	8	8	7	96.5	1.5	48.2	2.89	0.49	0.005, 1	B
8	8	16	7	96.5	1.5	24.1	2.65	0.04	0.05, 2	C
8	8	16	9	76.2	0.94	19.0	2.87	0.02	0.05, 2	D
							2.88			MKM

Each case computed used one of three meshes. The streamwise normal cross-section of each mesh is shown in Fig. 2, and the cases that used each mesh are listed. Mesh M2 was created from M1 by doubling the number of spanwise elements. Mesh M3 has the same number of elements as M2 but with order $N = 9$, instead of $N = 7$. Shown are all nthe spectral element nodes.

All cases are summarized in Table 1. Listed is the number of elements in each direction $E_x,\ E_y,\ E_z$; the order of spectral elements N; the maximum streamwise mesh spacing $\Delta x^+_{\max}$; the first grid point away from the wall y_1^+; the maximum spanwise mesh spacing $\Delta z^+_{\max}$; the mean wall shear stress $\tau_{w,m}$; the maximum deviation of τ_w from the mean; the filter level α; and number of modes filtered M. The values $(\cdot)^+$ shown in the table are normalized by the mean wall shear stress $\tau_{w,m}$ of MKM, so that cases calculated on the same mesh have the same wall coordinates, despite having different values of mean wall shear stress. However, in the figures presented all data have been normalized by the values of the corresponding calculation.

4.2.1 Effect of Filter

To examine the effect filter strength, we compare two setups of the same resolution. The high-filter case A had the filter parameters $\alpha = 0.050,\ M = 2$. The low-fiter case B had $\alpha = 0.005,\ M = 1$. These are summarized in Table 1.

In the spanwise wall shear stress profile (Fig. 3a), we clearly see the element boundaries at each spike. This effect is due to the lack of strong continuity requirements of the spectral element method at the element boundaries (Section 3). The wall shear stress τ_w is computed from the derivatives, which are not required to be continuous across element boundaries. We also see that the variation in the profile is of the same form but that the high filter shows a decrease in the magnitude of the spikes.

We quantify the effect of filtering on the wall shear stress τ_w by the maximum peak deviation from the mean in the spanwise variation of the wall shear stress $\Delta\tau_{\max} = \max_{x\in\Omega} |\tau_w(x) - \tau_{w,m}|/\tau_{w,m}$. The value is 28% for the high filter, and the value is 49% for the low filter. These values may seem to indicate that a higher filter is better. However, by comparing the mean wall shear stress values with the MKM case, we

see that this is not true. The high-filter case predicts $\tau_{w,m} = 2.46 \times 10^{-3}$, and the low-filter case predicts $\tau_{w,m} = 2.89 \times 10^{-3}$; according to MKM, $\tau_{w,m} = 2.88 \times 10^{-3}$. While greater filtering of the solution decreases the spikes in the streamwise variation of τ_w, it also inaccurately reduces the mean value.

The effects of a low value of $\tau_{w,m}$ are also noticed by looking at the mean streamwise velocity profile (Fig. 3b). Here we see that the underprediction of $\tau_{w,m}$ in the case of the high filter results in overpredicting the mean streamwise velocity. We also see that the low filter fits the expected law of wall quite well. However, using the mean wall shear stress as a measure of the fidelity of the result is not recommended because, as we see in the spanwise profile of τ_w, an accurate mean does not indicate that the result is correct throughout the domain.

4.2.2 Effect of Spanwise Resolution

We compare the effects of spanwise resolution by considering cases A, C, and D, where the filtering is the same but the mesh parameters change. Case C has had the number of spanwise elements doubled, and case D has further had the order increased from $N = 7$ to $N = 9$. The increase in elements improved $\tau_{w,m}$ modestly, raising it from 2.46 to 2.65. However, it reduced the spikes in τ_w from $\Delta\tau_{\max} = 0.28$ to $\Delta\tau_{\max} = 0.04$. The mean streamwise profile is improved marginally. The increase in element order from case C to case D further reduces $\Delta\tau_{\max}$, while predicting a $\tau_{w,m}$ very close to the DNS value. The mean streamwise profile of D is also very close to the expected value.

The turbulent kinetic energy $k^+ = \frac{1}{2}(\overline{u^2} + \overline{v^2} + \overline{w^2})/u_\tau^2$ is calculated for each setup and shown in Fig. 3d alongside the MKM data. Another effect of underresolution can be observed in the overprediction of k^+ near the wall. The effect is substantial in the underresolved cases A and C. In the more resolved case D, k^+ only slightly overpredicts the peak. In all cases, k^+ is underpredicted away from the wall. Also, one can see in Fig. 3d an indicator of the lack of resolution in the y direction; the turbulent kinetic energy contains peaks in case A near element boundaries at $y^+ \approx 140$ and $y^+ \approx 320$, similar to what was seen with the wall shear stress.

While streamwise and wall-normal resolution has been increased from case C to case D, the spanwise variation in the mean value of the wall shear stress is most heavily dependent on the spanwise resolution. In the following section, the stress will be shown to vary little with the streamwise resolution. In fact, the resolution in the streamwise direction will affect the streamwise variation of the wall shear stress, but that is not primary focus of the present comparisons.

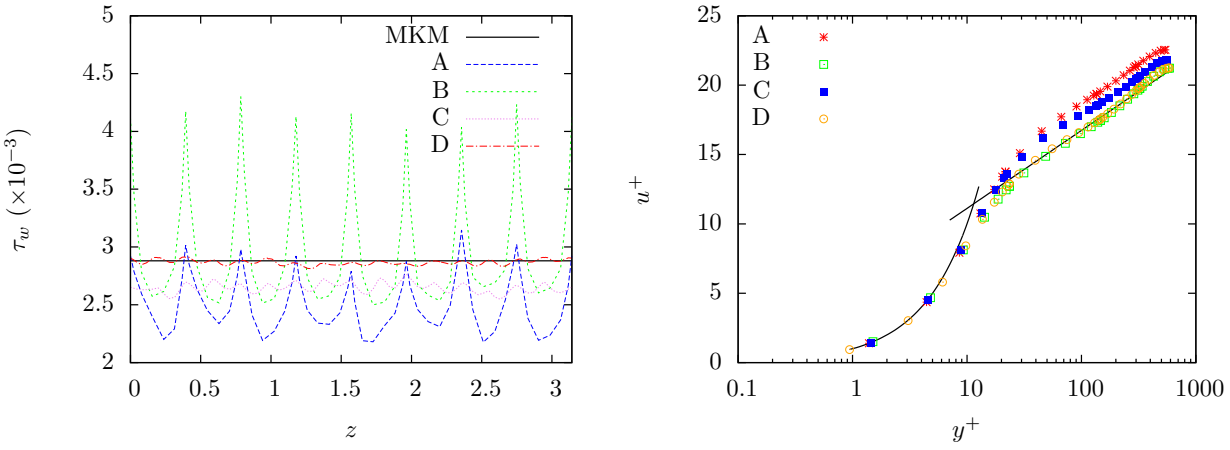

(a) Spanwise wall shear stress

(b) Mean velocity profile

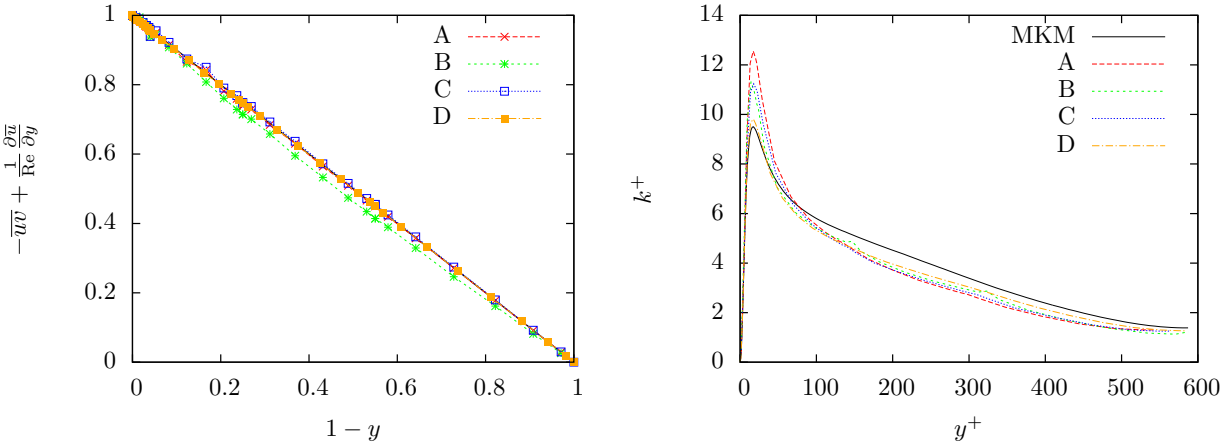

(c) Total shear stress

(d) Turbulent kinetic energy, k^+

Figure 3: High-filter and low-filter cases.

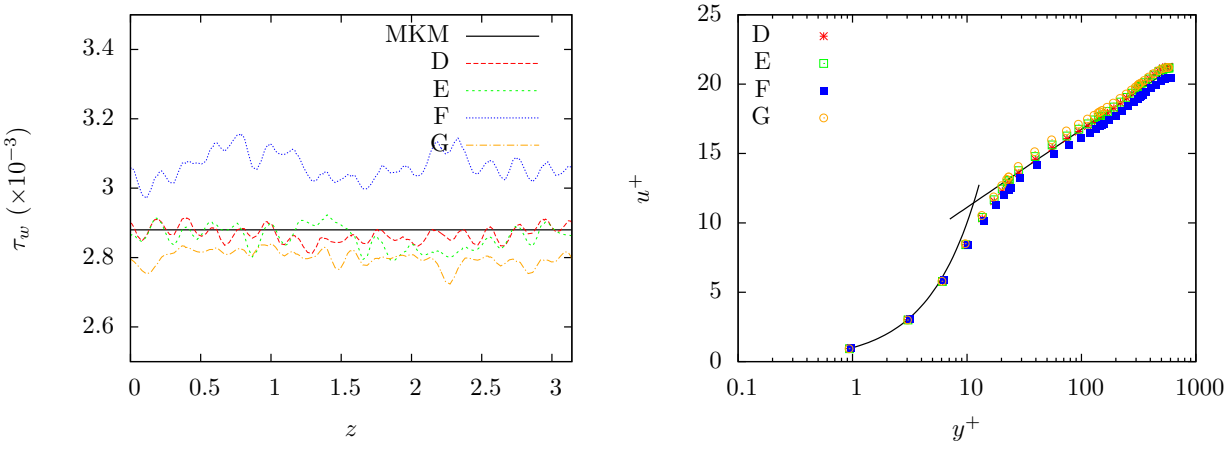

(a) Spanwise wall shear stress

(b) Mean velocity profile

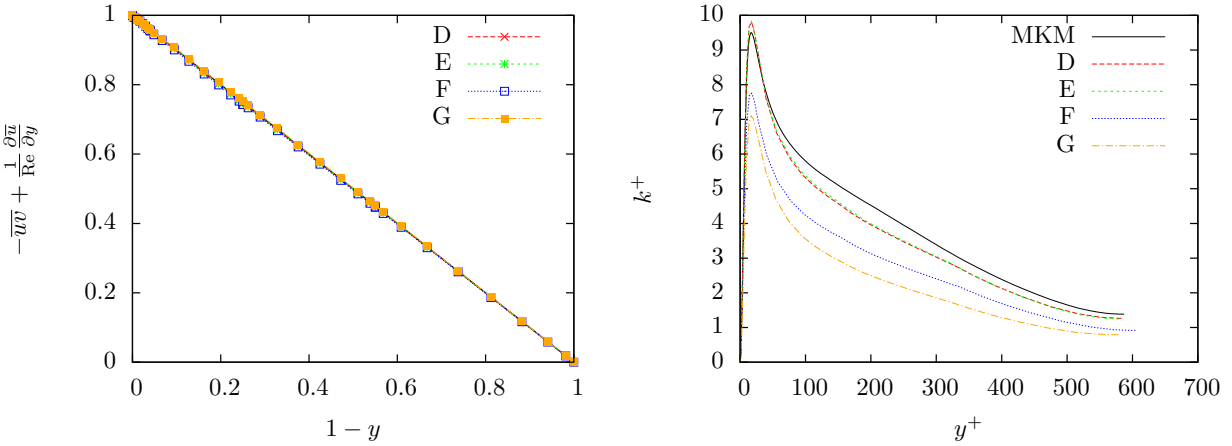

(c) Total shear stress

(d) Turbulent kinetic energy, k^+

Figure 4: Highest resolution mesh, stretched by a factor α_z. Cases E and F have $\alpha_z = 5/4$, and case D has $\alpha_z = 3/2$. Additionally, case F has filtering turned off in wall elements.

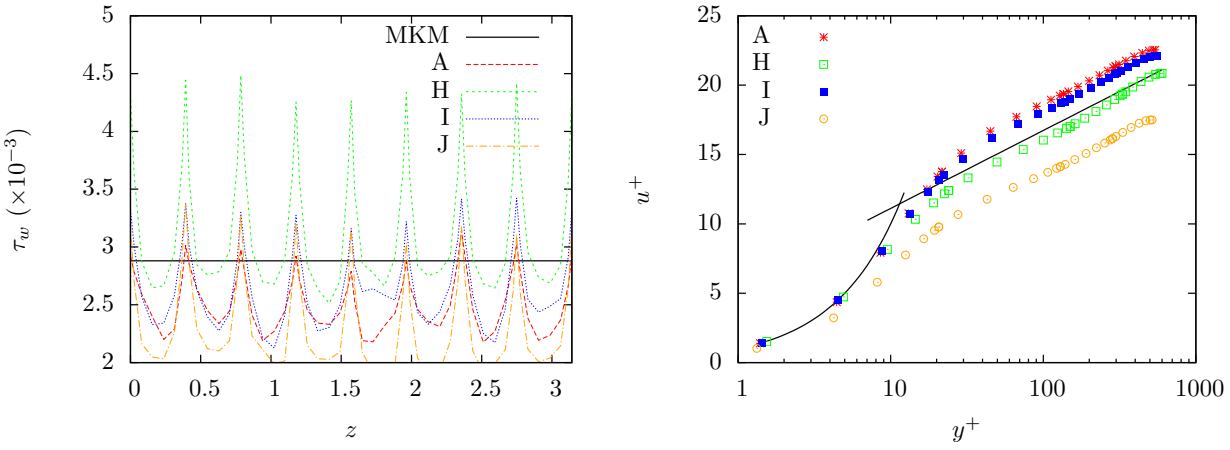

(a) Spanwise wall shear stress

(b) Mean velocity profile

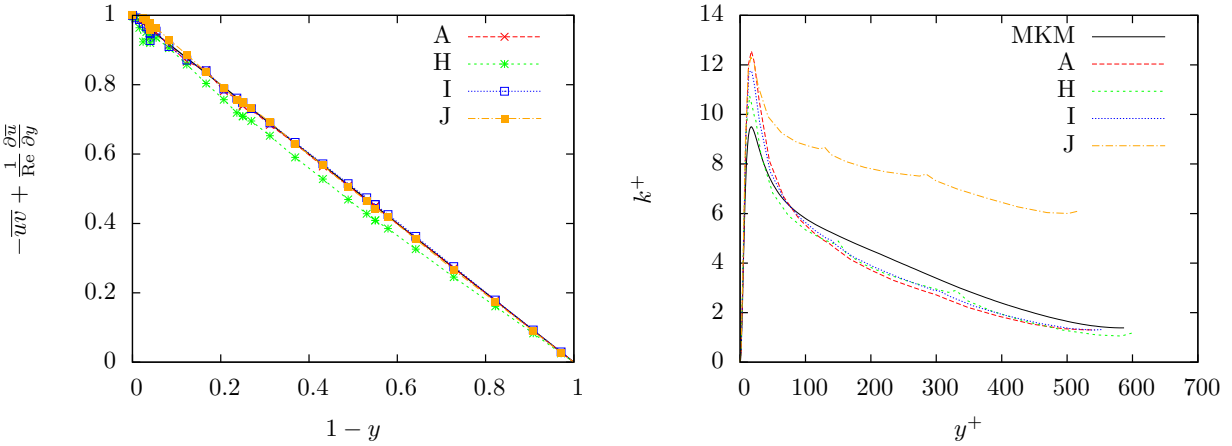

(c) Total shear stress

(d) Turbulent kinetic energy, k^+

Figure 5: Low-resolution mesh with various filters: A - standard Nek5000 filter with $\alpha = 0.05$, $M = 1$; H - dynamic Smagorinsky with van Driest damping; I - same as A but with no filtering in the spanwise direction; J - d4 filter with hyperviscosity formulation.

4.2.3 Streamwise Resolution

In addition to comparing the effects of spanwise resolution, we investigated the effects of decreasing the streamwise resolution of case D. Using the same mesh, we extended the domain in the streamwise direction by a factor α_z, reducing the streamwise resolution relative to case D by $1/\alpha_z$. The results of two cases of this kind are summarized in Table 2.

In cases E and G we see that the decrease in resolution leads to more filtering and, thus, a lower $\tau_{w,m}$. This was clear from considering the setups above. As a result, the mean profile is seen to lie above the expected law of the wall (Fig. 4a). We note that the effect is modest, even for a decrease in streamwise

resolution of 1/3. Cases E and G are still within the recommended level of resolution for an LES, indicating that within these bounds the quality of an LES does not vary strongly with streamwise resolution.

The effect of removing filtering along the boundary was also considered. This was achieved by manually turning off the filtering mechanism for all elements that touch the no-slip boundary. Case Fis this setup. We see that the $\tau_{w,m}$ is overpredicted. This overprediction leads to the mean streamwise velocity profile falling below the expected values (Fig. 4b). This result is likely due to the highest wavenumber, unstable modes gathering energy, since they are not removed by the filter.

4.2.4 SGS Models

To determine whether the mesh imprinting seen in the underresolved case was characteristic of the specific LES filter used, we simulated the channel flow with two other subgrid scale models and a modification of the standard Nek5000 spectral filter. The first, case H, used the dynamic Smagorinsky model with van Driest damping applied. The second, case I, used an anistropic spectral filter that applied only in the streamwise and wall-normal directions. The third, case J, used a hyperviscosity formulation.

We consider only the qualitative effects shown in Fig. 5. We notice that the results of the anisotropic filter in case I differ only slightly from case A. Case H produces results similar to the low-filter case B, where $\tau_{w,m}$ is slightly overpredicted and $\Delta\tau_{\max}$ is large. Case J is observed to be inaccurate.

The main observation is that the effect of underresolution is independent of the exact subgrid scale model used. The same mesh imprinting is seen in each case.

Table 2: Channel flow parameters for setups studied

$\mathrm{Re} = 10935,\ \mathrm{Re}_\tau = 590$				
α_z	$\Delta x^+_{\max}$	$\tau_{w,m}(\times 10^{-3})$	Filter at Wall Element?	Case
1	76.2	2.87	Y	D
5/4	95.3	2.86	Y	E
5/4	95.3	3.06	N	F
3/2	114	2.80	Y	G
		2.88		MKM

4.3 Discussion

For wall-resolved LES, the recommended level of resolution is usually given as [10, 23]

$$50 \leq \Delta x^+ \leq 150,\ \Delta y_1^+ < 1,\ 15 \leq \Delta z^+ \leq 40 \tag{11}$$

for "flat platelike" configurations where the x direction is streamwise, the y direction is wall normal, y_1^+ is the first point away from the wall, and the z direction is spanwise (homogeneous).

We have found that these recommendations were sufficient criteria to produce the correct mean streamwise velocity, total shear stress, and mean wall shear stress. However, they were not sufficient to correctly reproduce the wall shear stress across the entire spanwise direction. The cases with $\Delta z^+_{\max} = 48.2$ showed clear mesh imprinting on the wall shear stress values due to the local filtering within each element. For the cases with $\Delta z^+_{\max} \simeq 20$, we found that the spikes were greatly reduced. The most resolved case, which is well within the resolution guidelines, still showed minimal mesh imprinting in the wall shear stress. A more stringent requirement of $\Delta z^+_{\max} \leq 20$ is more appropriate for the resolution of a spanwise-varying quantity, such as τ_w. However, a requirement such as maximum grid spacing does not take into account the increased wave number resolution inherent in high-order methods. As demonstrated in Section 5, a higher order is preferable to a fine mesh.

We have also found that increased filter amplitudes are not effective in reducing the resolution requirements. In fact, while increasing the regularity of the solution, high-amplitude filters adversely affect the calculation by removing too much of the near-wall turbulent energy. The end result is less accurate mean flow values.

5 Rod Bundle Flow

Turbulent flow through rod bundles is composed of complex energy production and transport mechanisms that arise from the interactions of the flow with the walls and with gaps, leading to flow patterns similar to those found both in pipes and in compound channels joined by a narrow gap [2–4, 6, 11–14, 19–21, 26–29, 31]. The problem has been studied with numerous experiments and computations by the nuclear engineering community because of its application to safe and efficient nuclear hydraulic design.

In 1998, Krauss and Meyer, hereafter KM, published results of a systematic study they conducted on an experimental setup of a 37 rod bundle [16]. Their bundle consisted of an array of triangular pitch that they could vary. They reported on two studies in this bundle. In the one study, the rods were arranged with a pitch-to-diameter ratio of $P/D = 1.12$, wall-to-diameter ratio of $W/D = 1.06$, and bulk Reynolds number $\mathrm{Re_b} = 64590$. In the other study the parameters were $P/D = 1.06$, $W/D = 1.03$, and $\mathrm{Re_b} = 38754$. We are concerned with the former. In their study, they measured mean flow properties for both momentum and heat in a central channel of the rod bundle, including turbulence intensity of the velocities, turbulent kinetic

energy, wall shear stress, and Reynolds stresses. Measurements were made by hot wire anemometry using a three-wire probe. In further investigations, they provided substantial evidence for the existence of a gap vortex street responsible for strong interchannel mixing through the rod gaps.

5.1 Computational Model

In our study, we conducted calculations of the flow around a single rod in a periodic array. The domain and parameters were chosen to match those of a central rod in the bundle of the Krauss Meyer experiment and to contain two flow subchannels. The domain was periodic in the spanwise direction, so that opposite faces on the hexagon were connected. Streamwise periodicity is also used. The pitch-to-diameter ratio of the array was $P/D = 1.12$. Geometry and coordinates are shown in Figure 6. The Reynolds number was $\mathrm{Re} = 64590$ based on the hydraulic diameter D_h of one flow channel. The length of the domain was at least $L = 2\pi D_h$.[1] The time step in advective time units $t_a = D_h/U_b$ was $\Delta t = 0.0005\, t_a$.

Statistics were gathered over a time of 10-20 advective time units. Symmetries in the flow were used to further average the data of a minimal flow element. Therefore, the statistics were gathered over an effective time of 250-570 advective time units, depending on the particular case.

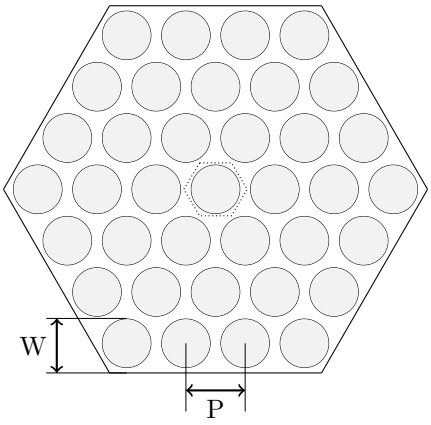

(a) Rod bundle configuration of Krauss and Meyer, with outline of single rod geometry indicated.

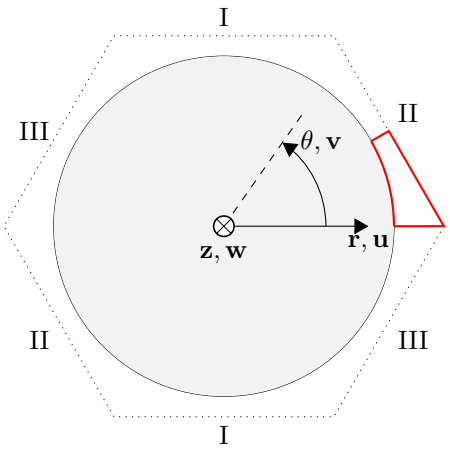

(b) Single rod in periodic array with periodicity in the plane labeled by I, II, III. Coordinate system and minimal flow element shown by the thick (red) line.

Figure 6: Cross-section of domain.

[1] Cases C, D, and E used domains of length $L = 8\pi D_h$ to shorten the time integration needed for statistics.

Table 3: Rod flow parameters for setups studied

Re = 64590, $P/D = 1.12$, Filter: $\alpha = 0.01$, $M = 1$								
E_r	E_θ	E_z	N	$r\Delta\theta^+_{\max}$	$\Delta z_{\max}$	y_1^+	$\tau_{w,m}(\times 10^{-3})$	case
3	6	13	19	33	136	0.71	2.93	A
6	10	24	11	34	121	0.35	2.75	B
6	39	25	11	8	118	0.62	2.82	C
3	15	15	19	13	119	0.62	2.83	D
3	12	15	23	13	98	0.42	2.83	E
							2.41	KM

5.2 Results

We compare the solutions of five different calculations with the experimental data. Parameters for the calculations are summarized in Table 3. All cases are compared in Fig. 7, where y is the radial distance from the wall of the rod $\hat{y}$ is the distance from the rod to the line of maximum velocity at $\theta = 0$. In addition, further results of the flow calculations are presented for Case D.

5.2.1 Effect of Polynomial Order

In order to compare the effectiveness of using higher-order spectral elements versus lower-order spectral elements, two different cases with the same number of points in the spanwise direction are compared. The higher-order case A consists of a mesh of 3 elements radially and 6 elements spanwise in the minimal flow element, all of order $N = 19$. The lower-order case B consists of a mesh of 6 elements radially and 10 elements spanwise in the minimal flow element, all of order $N = 11$.

The mean streamwise velocity profile is found to be robust to changes in the resolution. In Fig. 7b, we compare the mean in the radial direction at $\theta = 0$ for all cases computed with the log law reported by KM, $u^+ = 2.5 \ln y^+ + 4.5$. Case B is slightly closer than A, despite the higher order using only 60 points radially compared with the lower-order case using 72 points radially. This result indicates that the solution with fewer points, A, is close to spatial convergence already. Also, we see that the higher-order elements can effectively capture the same solution with fewer grid points.

In Fig. 7a, we see that the lower-order case has much greater spikes in τ_w over the the domain $\theta[^\circ] = [0, 30]$. We note that while the higher-order case is not averaged for a sufficient amount of time to reach statistical convergence, the spikes have been shown to persist at the element boundaries regardless of the sample sizes in other cases. This result indicates that there are higher order modes of the solution that are better resolved through increasing element order (p-refinement) rather than number of elements (h-refinement).

Additionally, with the same filter parameters $\alpha = 0.01, M = 1$ the higher-order case is effectively filtering away less energy from the domain. A reason is that the filter is applied only at the last few modes, which are greater in the higher-order case (i.e., the critical wavenumber k_c is higher with higher polynomial order).

5.2.2 Refinement Strategy

We now consider cases C, D, and E. Cases C and D used meshes that were refined by increasing the number of elements in the azimuthal direction near the wall. Away from the wall, the number of elements is smaller by a factor of 3 through the use of intermediate trapezoidal elements, shown in Fig. 8a. Case E does not employ this reduction away from the wall.

The main result of the refinement can be seen in Fig. 7a. Here we see that while C and D vary smoothly as θ, C begins to depart from the experimental data near $\theta = 10°$. The profile of C also varies almost linearly with θ, not as expected. It therefore overpredicts τ_w at $\theta = 0$ and underpredicts in the region $\theta = [13°, 20°]$. Case D is closer but deviates from the data at $\theta = 0$, $\theta = 12.5$, and $\theta = 30$. Case E is clearly the best. As noted in Table 3, the mean value of these three cases differs only slightly.

In all other measures shown, the three do not differ significantly. With regard to the total shear stress, they compare well to the expected value. The kinetic energy profile for all cases is similar.

5.2.3 Additional Results

Results for other flow properties are shown for case D.

The higher order moments at $\theta = 0$ are shown in Fig. 9. The wall-normal skewness behaves similarly to that of channel flow (KMM) near the wall, but far away from the wall it grows positively. The streamwise skewness varies significantly from channel flow, having two additional crossover points, near $y^+ \approx 105$ and $y^+ \approx 541$, where it takes on a small positive value. Above $y^+ = 541$, it maintains a negative value that varies with distance from the wall. One potential explanation for the region of positive skew would be the influence of ejection effects. However, these are seen in channel flow as well, without the positive skew. Another explanation is that within this geometry there exist secondary flows (Fig. 8b) exist that contribute to the bulk movement of slow speed of the fluid from the wall to the center of the subchannel. It is unclear whether either of these effects is methodical or physical, since the resolution away from the wall is relatively coarse. Further sampling does not affect the behavior.

In Fig. 10, the distribution of instantaneous measurements of (w', v') is plotted. The velocities have been normalized by the local shear velocity u_τ. We see that the near-wall turbulence is essentially two-

dimensional, especially near the wide gap. There is also a dominance of production events in the wide gap region compared with the narrow gap, for example at $y^+ \approx 52$ in the wide gap and $y^+ \approx 49$ in the narrow gap. The distribution of (w', v') becomes isotropic at smaller y^+ in the narrow gap.

Figure 11 shows the power spectra at the center of the narrow gap along with a line indicating the Kolmgorov spectrum. The frequency has been dimensionalized while the energy is scaled relative to the total. The spectrum indicates that the scales in the inertial range are properly resolved.

The components of the two-point correlation tensor in the narrow gap are shown in Fig. 12. The velocity signal seems to decorrelate in a short time frame, unlike what is observed for tighter rod bundles [19].

Low-speed streaks can be seen in a plot of velocity contours on a cylindrical surface at $y^+ \approx 2$ shown in Fig. 13. Streak spacing was found to be approximately $106y^+$. Approaching $\theta = 0$, the size of the streaks diminishes while the total number increases, indicating a significant increase in turbulence production.

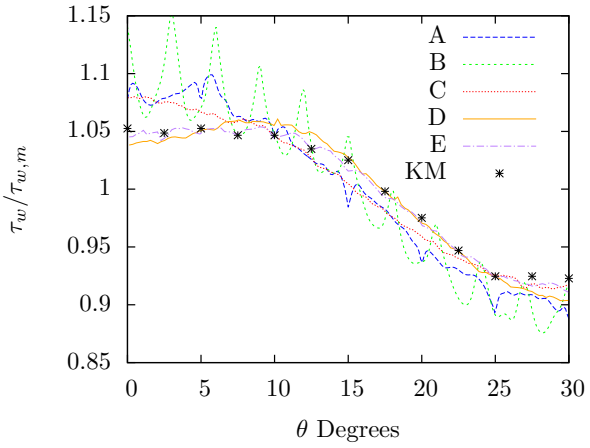

(a) Wall shear stress.

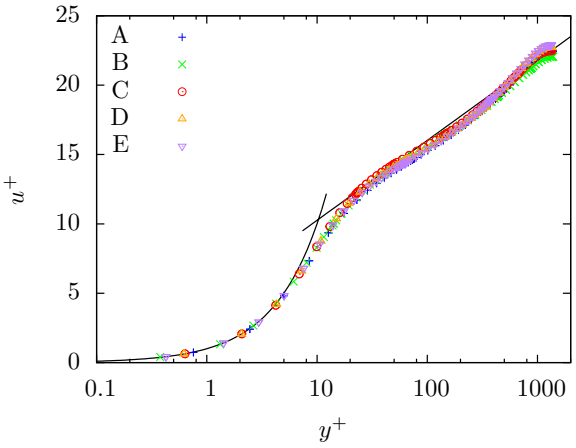

(b) Mean streamwise velocity.

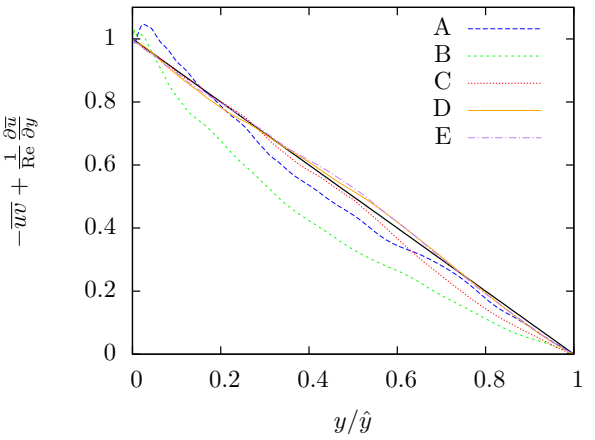

(c) Total shear stress.

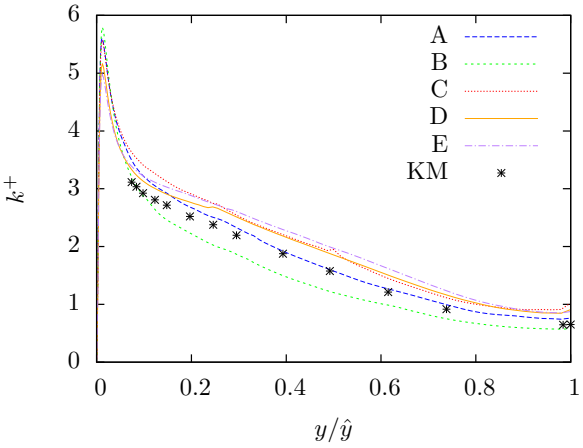

(d) Turbulent kinetic energy at $\theta = 0$.

Figure 7: Comparison of mean flow quantities.

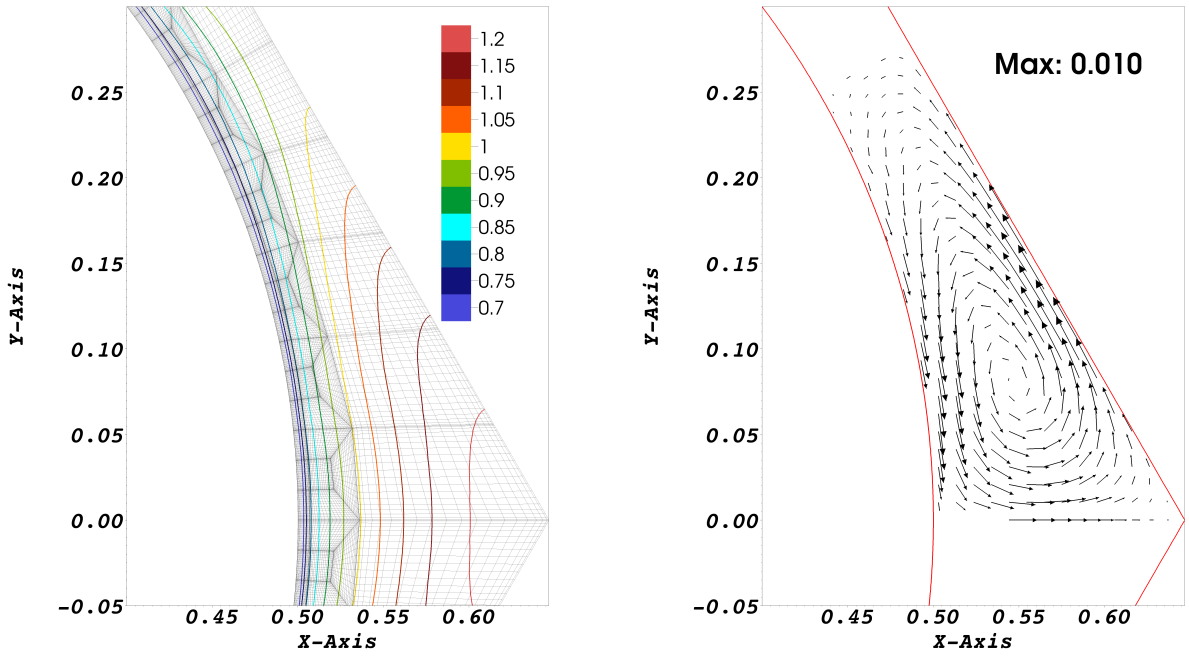

(a) Streamwise velocity

(b) Secondary flow

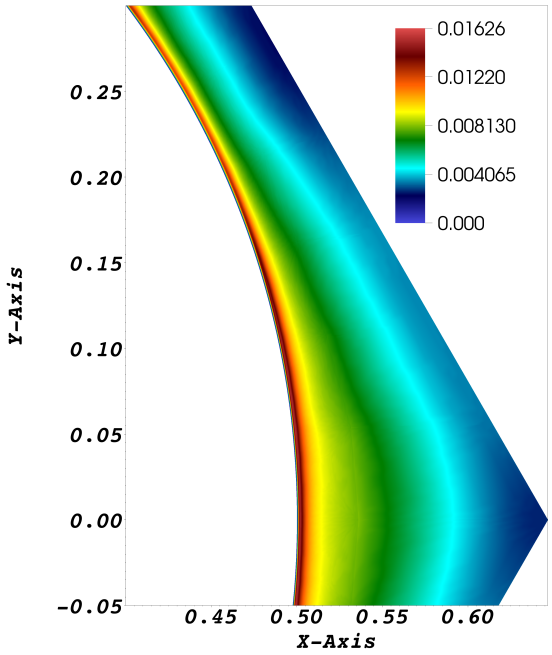

(c) Kinetic energy

Figure 8: Mean flow properties.

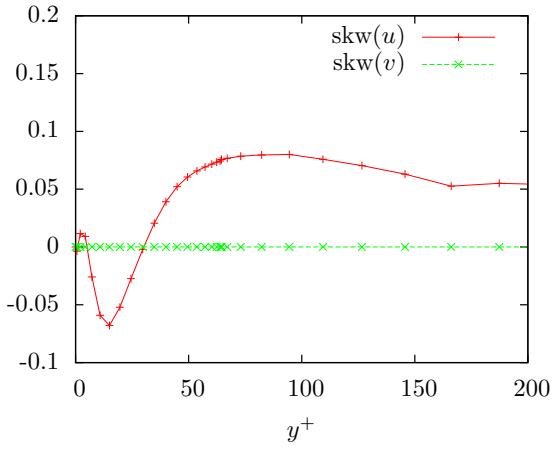

(a) Skewness for wall-normal and spanwise components.

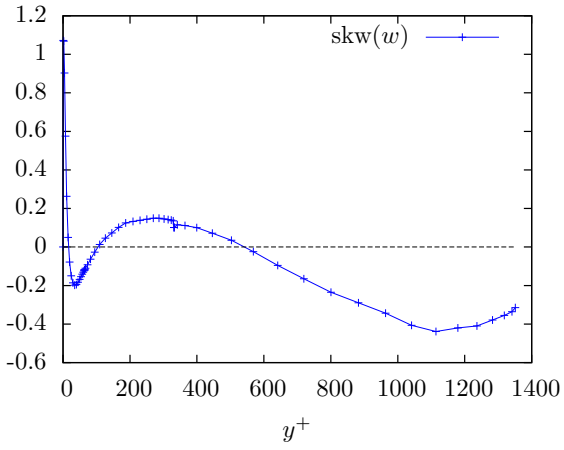

(b) Skewness for streamwise component.

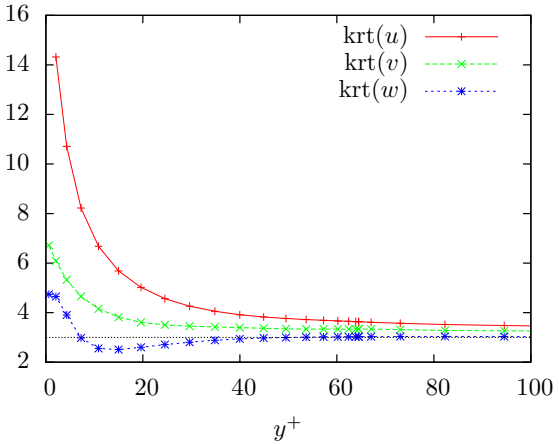

(c) Kurtosis for all three components.

Figure 9: Higher-order moments at $\theta = 0$.

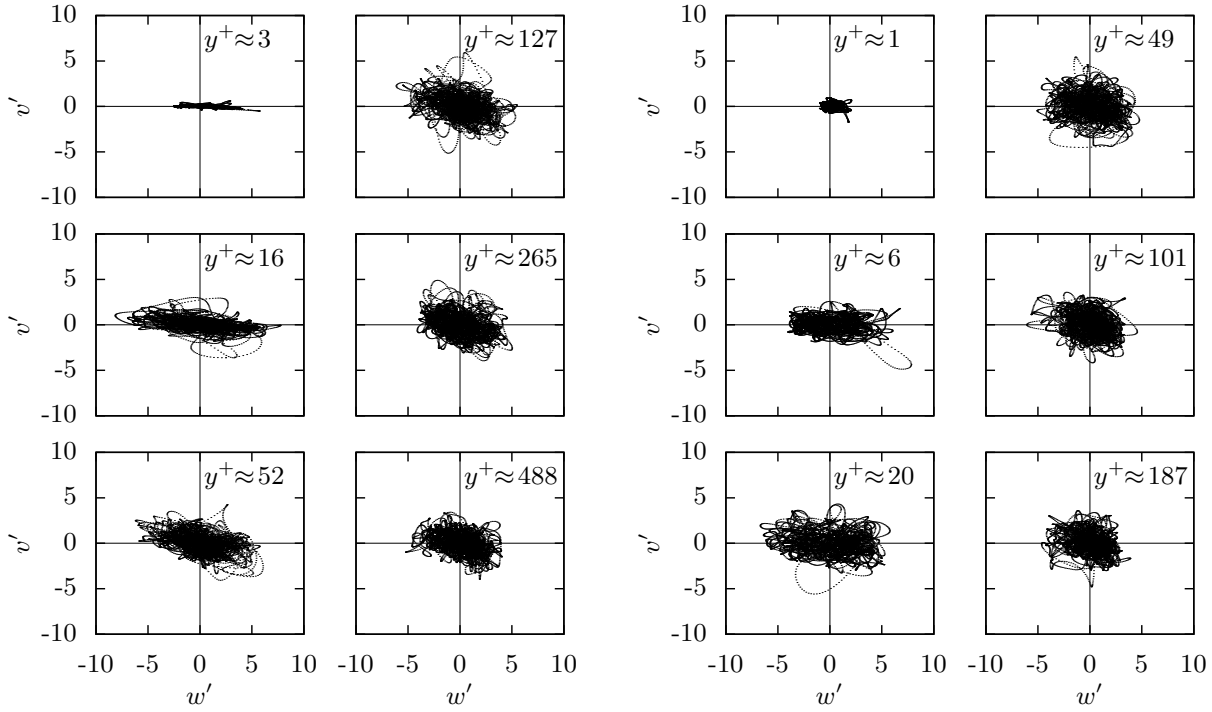

(a) Wide gap, $\theta = 0°$.

(b) Narrow gap, $\theta = 30°$.

Figure 10: Instantaneous (w', v').

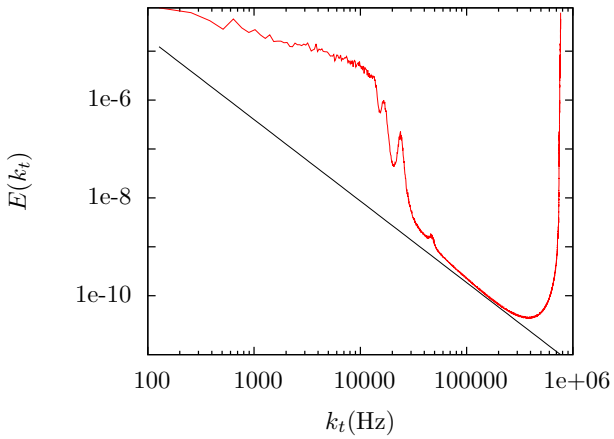

Figure 11: Auto spectral power density in narrow gap.

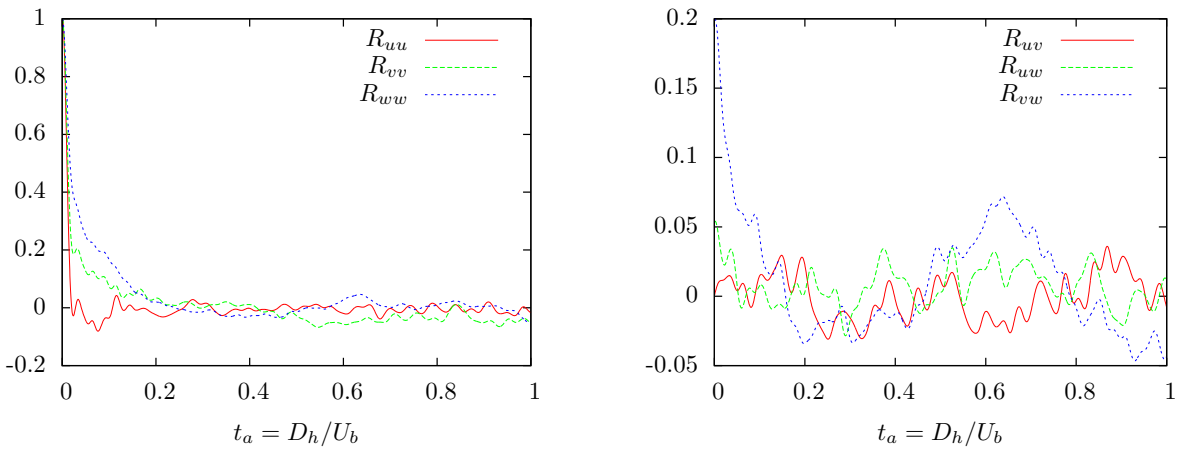

Figure 12: Two-point correlation coefficients in narrow gap.

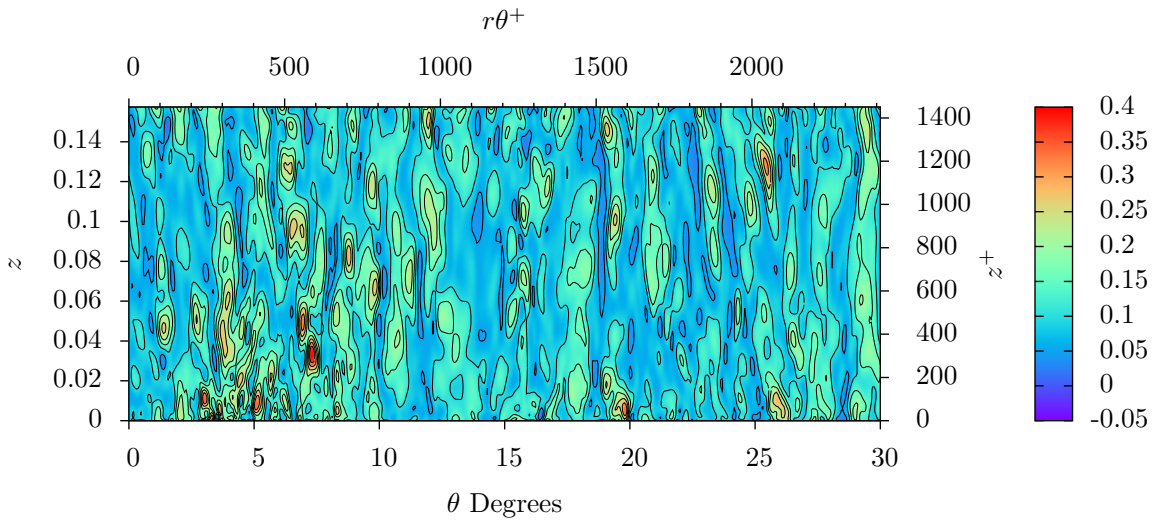

Figure 13: Streaks at $y^+ \approx 2$.

6 Conclusions

A series of simulations for channel flow and an infinite-array rod bundle have been conducted with the spectral element code Nek5000. The effort was aimed at reproducing correctly the flow field while exploring the resolution requirements to solve accurately the wall shear stress.

We have found that the recommendations usually provided for channel flow [10,23] were sufficient criteria to produce the correct mean streamwise velocity, total shear stress, and mean wall shear stress. However,

they were not sufficient to correctly reproduce the local wall shear stress in both rod bundles and channel flow.

In particular we found that the resolution in the direction where it is desired to resolve the local wall shear stress (e.g., spanwise in the present case) is crucial for producing accurate results. Such requirements lead to potentially much finer grids, if applied uniformly in the spanwise direction.

The use of very high-order basis functions is found to be preferable to low order. For lower orders the resolution requirements tend to be finer. The most accurate results in the case of the rod were produced for 23rd-order polynomials using nearly half as many points near the wall as a comparable 11th-order case.

A refinement strategy to maintain the resolution as coarse as possible in the bulk while meeting the resolution requirements in the near-wall region was devised (Fig. 8a). The simulations performed for a single pin calculation were in excellent agreement with available experimental results.

The present guidelines and refinement approach have been used to perform a 37 pin simulation. Such simulation will be used to analyze in the detail the structure of turbulence in rod bundles.

7 Acknowledgments

This work was supported in part by the Office of Advanced Scientific Computing Research, Office of Science, U.S. Dept. of Energy, under Contract DE-AC02-06CH11357.

Moreover, this research used resources of the Argonne Leadership Computing Facility at Argonne National Laboratory, which is supported by the Office of Science of the U.S. Department of Energy under contract DE-AC02-06CH11357.

References

[1] E. Baglietto and H. Ninokata. A turbulence model study for simulating flow inside tight lattice rod bundles. *Nuclear Engineering and Design*, 235(7):773–784, 2005.

[2] F. Barato, S. Bailey, and S. Tavoularis. Measurements of frequencies and spatial correlations of coherent structures in rod bundle flows. *Nuclear Engineering and Design*, 236:1830–1837, 2006.

[3] M. Biemuller, L. Meyer, and K. Rehme. Large eddy simulation and measurement of the structure of turbulence in two rectangular channels connected by a gap. In *Proc. 3rd Internat. Symp., Eng. Turbulence Modelling and Experiments*. Elsevier, 1996.

[4] D. Chang and S. Tavoularis. Numerical simullation of turbulent flow in a 37-rod bundle. *Nuclear Engineering and Design*, 237:575–590, 2007.

[5] M. Deville, P. Fischer, and E. Mund. *High-Order Methods for Incompressible Fluid Flow*. Cambridge Monographs on Applied and Computational Mathematics. Cambridge University Press, 2002.

[6] W. Eifler and R. Nijsing. Experimental investigation of velocity distribution and flow resistance in a triangular array of parallel rods. *Nuclear Engineering and Design*, 5:22–42, 1967.

[7] P. Fischer. An overlapping Schwarz method for spectral element solution of the incompressible Navier-Stokes equations. *Journal of Computational Physics*, 1997.

[8] P. Fischer and J. Mullen. Filter-based stabilization of spectral element methods. *Comptes rendus de l'Academie des sciences, Serie I Analyse numerique*, 332:265–270, 2001.

[9] P. F. Fischer, J. W. Lottes, and S. G. Kerkemeier. Nek5000 Web page, 2008. http://nek5000.mcs.anl.gov.

[10] N. J. Georgiadis, D. P. Rizzetta, and C. Fureby. Large-eddy simulation: Current capabilities, recommended practices, and future research. Technical Memorandum NASA/TM-2009-215616, NASA, NASA Center for Aerospace Information, 7115 Standard Drive, Hanover, MD 21076-1320, July 2009.

[11] A. Gosset and S. Tavoularis. Laminar flow instability in a rectangular channel with a cylindrical core. *Physics of Fluids*, 18(4):044108, 2006.

[12] M. Guellouz and S. Tavoularis. Heat transfer in rod bundle subchannels with varying rod-wall proximity. *Nuclear Engineering and Design*, 132:351–366, 1992.

[13] J. Hooper. Developed single phase turbulent flow through a square-pitch rod cluster. *Nuclear Engineering and Design*, 60:365–379, 1980.

[14] J. Hooper and K. Rehme. Large-scale structural effects in developed turbulent flow through closely-spaced rod arrays. *Journal of Fluid Mechanics*, 145:305–337, 1984.

[15] J. Kim, P. Moin, and R. Moser. Turbulence statistics in fully developed channel flow at low Reynolds number. *Journal of Fluid Mechanics*, 177:133–166, 1987.

[16] T. Krauss and L. Meyer. Experimental investigation of turbulent transport of momentum and energy in a heated rod bundle. *Nuclear Engineering and Design*, 180:185–206, 1998.

[17] Y. Maday, A. Patera, and E. Ronquist. An operator-integration-factor splitting method for time-dependent problems: Application to incompressible fluid flow. *Journal of Scientific Computing*, 5:263–292, 1990.

[18] E. Merzari and H. Ninokata. Proper orthogonal decomposition of the flow in a tight lattice rod-bundle. *Nuclear Engineering and Design*, 241(11):4621–4632, 2011. 13th International Topical Meeting on Nuclear Reactor Thermal Hydraulics.

[19] E. Merzari, H. Ninokata, and E. Baglietto. Numerical simulation of flows in tight-lattice fuel bundles. *Nuclear Engineering and Design*, 238:1703–1719, 2008.

[20] S. Möller. On phenomena of turbulent flow through rod bundles. *Experimental Thermal an Fluid Science*, 4(1):25–35, 1991.

[21] S. Möller. Single-phase turbulent mixing in rod bundles. *Experimental Thermal an Fluid Science*, 5(1):26–33, 1992.

[22] R. D. Moser, J. Kim, and N. N. Mansour. Direct numerical simulation of turbulent channel flow up to $\mathrm{Re}_\tau = 590$. *Physics of Fluids*, 11(4):943–945, April 1999.

[23] U. Piomelli and E. Balaras. Wall-layer models for large-eddy simulation. *Annual Reviews of Fluid Mechanics*, 34:349–374, January 2002.

[24] S. B. Pope. *Turbulent flows*. Cambridge university press, 2000.

[25] K. Rehme. *Convective Heat Transfer over Rod Bundles*, chapter 7. John Wiley & Sons, 1987.

[26] K. Rehme. The structure of turbulent flow through rod bundles. *Nuclear Engineering and Design*, 99:141–154, 1987.

[27] W. J. Seale. Turbulent diffusion of heat between connected flow passages. *Nuclear Engineering and Design*, 54:183–195, 1979.

[28] W. J. Seale. Turbulent diffusion of heat between connected flow passages. *Nuclear Engineering and Design*, 54:197–209, 1979.

[29] W. J. Seale. Measurements and predicitions of fully developed turbulent flow in a simulated rod bundle. *Journal of Fluid Mechanics*, 123:399–423, 1982.

[30] C. team. The Cesar Codesign Center: Early results. In *DOE Exascale Conference*, 2012. https://cesar.mcs.anl.gov/sites/cesar.mcs.anl.gov/files/Technical

[31] A. C. Trupp and R. S. Azad. The structure of turbulent flow in triangular array rod bundles. *Nuclear Engineering and Design*, 32(1):47–84, 1975.